Article

Soil Moisture Monitoring at Kilometer Scale: Assimilation of Sentinel-1 Products in ISBA

Oscar Rojas-Munoz [1], Jean-Christophe Calvet [1,*], Bertrand Bonan [1], Nicolas Baghdadi [2], Catherine Meurey [1], Adrien Napoly [1], Jean-Pierre Wigneron [3] and Mehrez Zribi [4]

1 CNRM, Université de Toulouse, Météo-France, CNRS, 31057 Toulouse, France; oscar.rojas@meteo.fr (O.R.-M.); bertrand.bonan@meteo.fr (B.B.); adrien.napoly@meteo.fr (A.N.)
2 INRAE, UMR TETIS, Université de Montpellier, AgroParisTech, 34093 Montpellier, France; nicolas.baghdadi@inrae.fr
3 INRAE, UMR ISPA, Université de Bordeaux, 33140 Villenave d'Ornon, France; jean-pierre.wigneron@inrae.fr
4 CESBIO (CNES/CNRS/IRD/INRAE/UPS), 31401 Toulouse, France; mehrez.zribi@ird.fr
* Correspondence: jean-christophe.calvet@meteo.fr

Abstract: Observed by satellites for more than a decade, surface soil moisture (SSM) is an essential component of the Earth system. Today, with the Sentinel missions, SSM can be derived at a sub-kilometer spatial resolution. In this work, aggregated 1 km × 1 km SSM observations combining Sentinel-1 (S1) and Sentinel-2 (S2) data are assimilated for the first time into the Interactions between Soil, Biosphere, and Atmosphere (ISBA) land surface model using the global Land Data Assimilation System (LDAS-Monde) tool of Meteo-France. The ISBA simulations are driven by atmospheric variables from the Application of Research to Operations at Mesoscale (AROME) numerical weather prediction model for the period 2017–2019 for two regions in Southern France, Toulouse and Montpellier, and for the Salamanca region in Spain. The S1 SSM shows a good agreement with in situ SSM observations. The S1 SSM is assimilated either alone or together with leaf area index (LAI) observations from the PROBA-V satellite. The assimilation of S1 SSM alone has a small impact on the simulated root zone soil moisture. On the other hand, a marked impact of the assimilation is observed over agricultural areas when LAI is assimilated, and the impact is larger when S1 SSM and LAI are assimilated together.

Keywords: Sentinel-1; data assimilation; soil moisture; leaf area index

1. Introduction

Active and passive satellite-based microwave observations provide valuable tools for monitoring soil moisture, with the potential to provide global coverage at a high spatial and temporal resolution. Over the past decades, several satellite missions have been launched (e.g., ASCAT (Advanced Scatterometer) [1] and SMOS (Soil Moisture and Ocean Salinity) [2]), resulting in the development of a number of soil moisture products with different temporal and accuracy characteristics. These products have low spatial resolution, typically no better than 10 km, and are used for large-scale applications, including drought monitoring, flood forecasting, climate monitoring, and agricultural management [3–6]. The accuracy and reliability of satellite-based soil moisture products depend on several factors, including the satellite sensor design, retrieval algorithms, validation techniques, and vegetation structure [7]. There is a need to improve the spatial resolution of satellite-derived surface soil moisture (SSM) products and to evaluate their assimilation into land surface models (LSMs) [8]. One way to achieve this goal is to downscale already existing low-resolution SSM products to the kilometer scale by integrating local information from land cover or in situ measurements through machine learning [9]. Another way is to take advantage of recently developed satellite-based SSM products based on high-resolution Sentinel-1 (S1) C-band backscatter in conjunction with Sentinel-2 (S2) vegetation indices [10–13].

LSMs are used to simulate the diurnal and seasonal cycles of energy, water, and carbon fluxes at the soil–plant interface with the atmosphere at different spatial scales (from 0.1 to 100 km) worldwide. LSMs are capable of simulating physical and biological processes, such as photosynthesis and vegetation phenology, as well as soil moisture and soil temperature, for multiple soil layers [14,15]. In LSMs, sub-grid heterogeneity can be represented by patches, where each patch represents a different land cover type (such as forest, grassland, or cropland) and a range of physical characteristics (such as the plant rooting depth). The ISBA (Interactions between Soil, Biosphere, and Atmosphere) land surface model [16] is designed to be used in a variety of applications, either coupled with the atmosphere in climate and numerical weather prediction atmospheric models or offline (without interactions with the atmosphere). In the most advanced versions of ISBA, the leaf area index (LAI), a key vegetation state variable controlling carbon and water fluxes, is computed together with photosynthesis. The "A-gs" ISBA-A-gs configuration of ISBA [17–19], hereafter referred to as ISBA-A-gs, is used in this study. Accurate simulation of SSM and root zone soil moisture (RZSM) in addition to LAI is critical, as these variables control the partitioning of energy and water fluxes between the land surface and the atmosphere [20–22]. The measurement of soil moisture is challenging, especially at regional and global scales [23–25], leading to difficulties in evaluating RZSM.

The assimilation of satellite-derived SSM data together with LAI into LSMs aims to improve the accuracy and predictive ability of LSMs [26–28]. Kalman filtering techniques can be used to integrate these satellite-based observations into model simulations [29–32]. In the case of ISBA-A-gs, the joint assimilation of SSM and LAI products can be performed within the SURFEX (SURface Externalisée [33]) modeling platform, over France and on a global scale. The Land Data Assimilation System (LDAS) integrating satellite products in ISBA-A-gs is called LDAS-Monde [34] and produces modeled and analyzed variables (such as SSM, RZSM, LAI, evapotranspiration, and gross primary production (GPP)). Since ISBA-A-gs is not a crop model, it has shortcomings over agricultural areas, and the assimilation has a marked positive impact on the simulations [34]. As a baseline, LDAS-Monde is capable of assimilating LAI and SSM satellite products.

The objective of this paper is to (1) validate an aggregated 1 km × 1 km S1 SSM product and (2) evaluate, for the first time, the effect of assimilating S1 SSM in ISBA-A-gs at the kilometer scale using the LDAS-Monde tool driven by a high-resolution atmospheric forcing. The study was carried out in two regions in France and one region in Spain where in situ measurements of soil moisture are available. The assimilation of S1 SSM products alone, LAI alone, and S1 SSM together with LAI was performed in order to assess the added value of the S1 SSM assimilation.

The paper is organized as follows: Section 2 presents the ISBA model and the LDAS-Monde tool, the satellite and in situ datasets, as well as the study areas. Section 3 describes the methodology and the experimental design. Section 4 evaluates the S1 SSM products using in situ measurements of SSM and presents the assimilation results. Section 5 contains a discussion about how results can be interpreted. Section 6 provides conclusions and highlights on future works.

2. Model and Data

2.1. The ISBA LSM

The ISBA LSM is used to simulate the interactions between land surfaces and the lower atmosphere by resolving the energy and water balances at the surface level within the SURFEX (SURface Externalisée) modeling platform developed by the Centre National de Recherches Météorologiques (CNRM) (http://www.umr-cnrm.fr/surfex, accessed on 30 August 2023). Within SURFEX, ISBA generates a set of simulated variables, including heat, carbon, water, and energy surface fluxes, either coupled to an atmospheric model or "offline", i.e., without coupling to the atmosphere. In this study, version 8.1 of SURFEX was used in the offline mode. The atmospheric forcing came from the AROME-France (Application of Research to Operations at Mesoscale) numerical weather prediction model

of Meteo-France [35], which is run operationally at a spatial resolution of 1.3 km × 1.3 km over France [36].

Vegetation growth is represented in this study, using the ISBA-A-gs configuration [17,37]. This version of ISBA simulates the net CO_2 assimilation rate (A) and stomatal conductance (g_s) of vegetation at the leaf and canopy level, which allows the simulation of LAI, respiration, and energy and water fluxes. ISBA-A-gs is able to represent the feedbacks between LAI and soil RZSM: increasing LAI values tend to increase plant transpiration and to reduce RZSM through root water extraction, while decreasing RZSM values reduce photosynthesis, g_s, and LAI at some stage. To better represent RZSM, the ISBA diffusion multilayer representation of the soil [38,39] was used. Soil moisture and soil temperature were calculated for 14 layers down to 12 m for soil temperature and 8 to 10 layers down to 1 m and 2 m for soil moisture, depending on vegetation characteristics. In this study, the WG2 and WG5 modeled soil moisture values were considered. They correspond to the ISBA soil layers 2 and 5, 0.01–0.04 m and 0.2–0.4 m, respectively. They can be considered as proxies for SSM and RZSM, respectively. The ISBA model version we used does not include irrigation.

2.2. LDAS-Monde

Within the SURFEX modeling platform, the joint assimilation of SSM and LAI satellite-based products is possible using the LDAS-Monde tool. LDAS-Monde assimilates satellite products using a simplified extended Kalman filter (SEKF) technique. The variables analyzed were LAI and soil moisture at several depths (up to 1 m). Each analyzed variable had 12 different values corresponding to 12 land surface patch classes. The patch fraction for each model grid cell was calculated from the ECOCLIMAP-II land cover database [40], including bare soil, rocks, permanent snow, and ice surfaces, and nine plant functional types (needleleaf trees, evergreen broadleaf trees, deciduous broadleaf trees, C3 crops, C4 crops, C4 irrigated crops, C3 grasslands, C4 grasslands, and wetlands). The assimilation process was performed every 24 h, and the analyzed variables were used as initial conditions for the next 24 h window. Instead of calculating each variable at the beginning of each cycle, they were adjusted based on available observations and their relative errors. LDAS-Monde has been already used in several studies to assimilate and validate different satellite products over different regions and at different scales (e.g., [34,41–44]). In this study, LDAS-Monde was adapted to the kilometer scale.

2.3. S1 SSM Data

In this study, SSM products were derived from the Sentinel-1A (S1A) and Sentinel-1B (S1B) C-band (wavelength: ~6 cm) backscatters. S1A was launched in April 2014 and S1B was launched two years later in April 2016. Both of them provide images with a spatial resolution of 10 m × 10 m. With two satellites in operation, the average sampling time is six days, in both ascending and descending modes over different regions of the globe. The obtained images were used to develop soil moisture maps, using a neural network approach involving inversion of radar signals, S^2MP (Sentinel-1/Sentinel-2 derived soil Moisture at Plot scale), as described in [10]. The retrieval process was applied to S1 backscatter in VV polarization (vertical transmit and vertical receive), in conjunction with NDVI (normalized difference vegetation index) time series derived from S2. It should be noted that SSM retrievals were not produced over straw cereal crops (mainly wheat and barley) during the spring stem elongation phase (due to the low penetration of the S1 wave in the canopy), forests, vineyards, and orchards. Land cover maps, cropland masks, and cropland and herbaceous vegetation masks at 100 m spatial resolution were derived for each year from the Copernicus Global Land Service dynamic land cover map (CGLS-LC100) (see Section 2.5). These maps were also used to aggregate SSM at 1 km × 1 km spatial resolution. First, the SSM values at the 100 m × 100 m spatial resolution were estimated using the grid of the land cover map, in order to avoid mixing several crop types within the same 1 km × 1 km grid scale in the average value of the S1 radar signal and NDVI. Second,

the obtained SSMs at the 100 m scale (only for cropland and herbaceous vegetation pixels) were averaged within each 1 km grid cell to obtain 1 km × 1 km SSM estimates.

The generated soil moisture maps (in $m^3 m^{-3}$), hereafter referred to as S1 SSM, cover three regions for a time period of three years, from January 2017 to December 2019, with two of them situated in the southern part of France and the other one located in the western part of Spain, as illustrated in Figure 1. The first region encompasses a rectangular area covering the region of Toulouse and measuring 211 × 293 km. The second region, Montpellier, has a rectangular area of 112 × 154 km. The Salamanca region in Spain covers an area of 246 × 319 km. Soil moisture measurement stations, which are presented in Section 2.4, are available within each region. The domain coordinates of Montpellier, Toulouse, and Salamanca are 43.254°–44.263°N and 2.987°–4.379°E, 43.245°–45.147°N and 0.469°–3.112°E, and 40.353°–42.567°N and 6.790°–3.924°W, respectively.
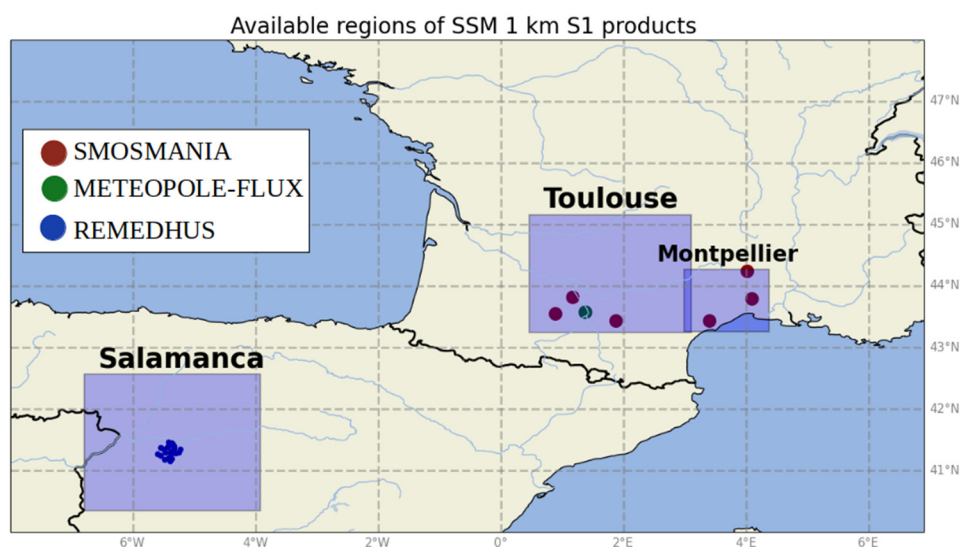

Figure 1. Salamanca, Toulouse, and Montpellier regions where S1 SSM products are available. In situ stations (REMEDHUS, Meteopole-Flux, and SMOSMANIA) are represented by dots.

Figure 2 shows S1 SSMs for a particular day in early May 2018 at approximately 18:00 UTC for the three regions described above. Note that it was not possible to display SSM for the three regions for the exact same day due to the temporal resolution of S1. The Toulouse region exhibited remarkable moist conditions on 8 May 2018, especially towards the southwest, with SSM values reaching as high as 0.28 $m^3 m^{-3}$. Local rainfall observations show that intense precipitation occurred in the morning of 8 May 2018. Conversely, the Montpellier region showed a greater spatial heterogeneity in SSM values on 3 May 2018. In the case of Salamanca, the prevailing conditions were dryer, with SSM values ranging between 0.06 and 0.10 $m^3 m^{-3}$. Note that the red and blue points marked on these maps correspond to the locations of SSM in situ measurements that are described in the following subsection.

As part of the assimilation process, it is necessary to rescale the S1 SSM products to match the ISBA model climatology and to avoid any bias in the system associated with model-dependent soil parameters, as described in [45,46]. To achieve this, the S1 SSM product was rescaled using the method proposed by [47], which involves a linear transformation that aligns the modeled SSM mean and variance with the estimated mean and variance of the observations. This linear transformation was applied on a seasonal basis using a three-month sliding window, as seasonal variability has been shown to significantly affect the rescaling process, as reported in [30,48,49]. In addition, a filter was applied to exclude urban areas and soil freezing before the rescaling parameters were estimated.
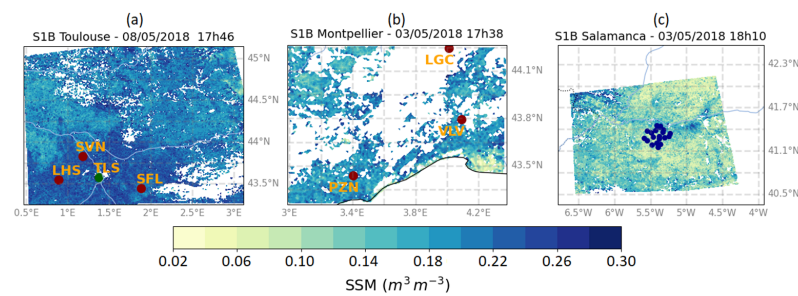
Figure 2. S1 SSM product maps for one day in May around 18:00 UTC for (**a**) Toulouse, (**b**) Montpellier, and (**c**) Salamanca. SMOSMANIA and REMEDHUS stations are represented by red and blue dots, respectively. The Meteopole-Flux station is represented by a green dot. White is used to mask missing data.

2.4. LAI Data

The GEOV1 LAI product is distributed by the Copernicus Global Land Service (CGLS). It is a satellite-based estimate of LAI that is derived from observations from the PROBA-V satellite. The product is generated using a statistical algorithm [50], specifically, a neural network trained on two other pre-existing products, and is provided globally with a spatial resolution of 1 km × 1 km and a sampling time of 10 days.

2.5. Land Cover

The land cover data were obtained from the global CGLS dataset based on PROBA-V observations at a spatial resolution of 100 m × 100 m. Since the S^{2}MP inversion model is only applicable to agricultural areas and grasslands (vineyards and orchards are excluded), the CGLS-LC100 map was filtered to retain only the agricultural areas listed in CGLS-LC100: cropland (map code "40") and herbaceous vegetation (map code "30"). In CGLS-LC100, cropland is defined as land covered with temporary crops followed by harvest and a period of bare soil. Note that perennial woody crops are classified as the appropriate forest or shrub land cover type. Herbaceous vegetation is defined in CGLS-LC100 as follows: "Plants without persistent stems or shoots above ground and lacking a definite firm structure (tree and shrub cover is less than 10%)".

Figure 3 shows the land cover classification for the Montpellier region. This region is mainly covered by open and closed forests, with cropland and urban areas located mainly in the south of the Mediterranean coast. Agricultural areas can also be found in the northeast of the region, around the city of Alès. The open forest and shrub classes may include crop fields, vineyards, and orchards. The global irrigation map of Meier et al. [51] shows that irrigation is common in this region.
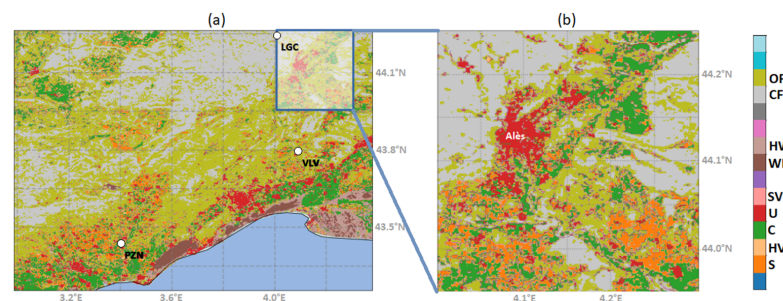

Figure 3. Land cover (CGLS) for (**a**) the Montpellier region and for (**b**) the Alès sub-domain (4°–4.3°E, 43.95°–44.25°N), including the city of Alès. Lands cover classes: open forest ("OF"), closed forest ("CF"), herbaceous wetland ("HW"), permanent water bodies ("WB"), sparse vegetation ("SV"), urban ("U"), cropland ("C"), herbaceous vegetation ("HV"), and shrubs ("S"). "OF" and "S" may include crop fields, vineyards, and orchards. The locations of the Pezenas, La Grand Combe, and Villevieille SMOSMANIA stations (PZN, LGC, and VLV, respectively) are shown.

2.6. In Situ Observations

The Soil Moisture Observing System–Meteorological Automatic Network Integrated Application (SMOSMANIA) is a network of weather stations with frequency domain reflectometry soil moisture sensors installed along a 400 km Mediterranean–Atlantic transect in Southern France, providing continuous measurements of soil moisture at different soil depths every 12 min from 2006 to the present [52]. In the two regions of France where S1 SSM products are available, there are three SMOSMANIA stations for the Toulouse region and three for the Montpellier region, as shown in Figure 2 (red dots). SSM is measured at a 5 cm soil depth.

In addition to the SMOSMANIA stations, SSM data are available from the Meteopole-Flux site within the Toulouse domain, as shown in Figure 2. This observatory is located on the Meteo-France campus in the southwest of Toulouse, France (43.57°N, 1.37°E; 158 m above sea level), and is designed to monitor atmospheric variables, energy, water, and CO_2 fluxes in real time, on a sub-hourly basis. Since June 2012, the Meteopole-Flux observatory has provided several meteorological variables, including in situ observations of soil moisture at different depths [53].

The REMEDHUS network is located in the Duero Basin in Spain, covering an area of 35 km × 35 km between the cities of Salamanca and Valladolid, and provides hourly observations of SSM at a 5 cm soil depth. The stations are located in the center of the Salamanca domain where S1 SSM products are available (blue dots in Figure 2). These instruments are located in a gently sloping hilly region at an altitude of 750–900 m above sea level and experience a semi-arid continental Mediterranean climate, where the land is mainly used for agricultural activities. Data from this network have been used in many studies to validate different satellite-derived observations [54–56]. In the context of this study, data from 19 stations were used for the period 2017–2019.

The SMOSMANIA [52] and REMEDHUS [57] data are available from the International Soil Moisture network (ISMN) [58].

It must be noticed that there is a mismatch between the in situ SSM observations at a 5 cm soil depth and the smaller C-band penetration depth of 1 to 2 cm [59].

3. Method

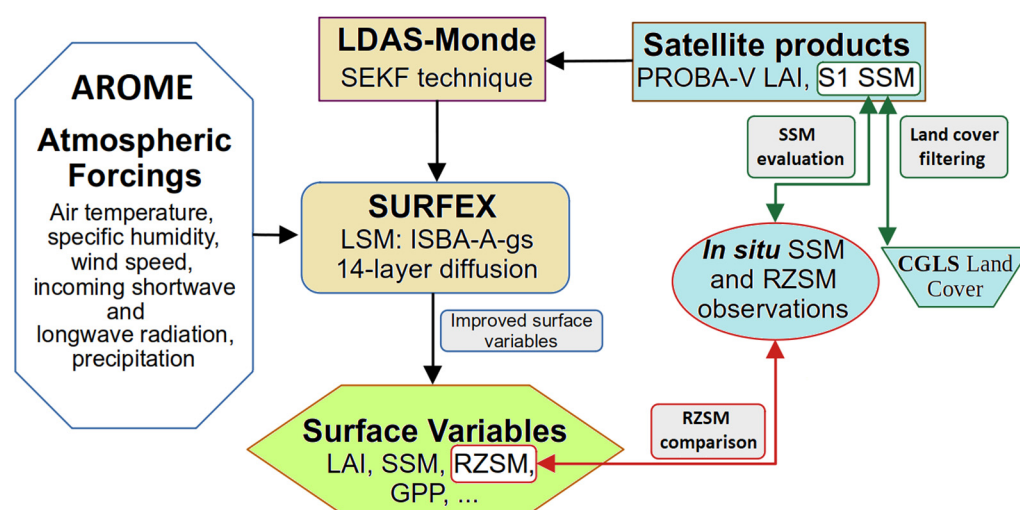The workflow of the proposed method is presented in Figure 4.

Figure 4. Method used to analyze root zone soil moisture (RZSM) by assimilating PROBA-V LAI and S1 SSM satellite observations into the ISBA land surface model. In situ SSM and RZSM observations were used to evaluate S1 SSM and the analyzed RZSM, respectively.

3.1. Experimental Set Up

The numerical experiments performed in this study are summarized in Table 1. LDAS-Monde was set up in the same configuration for the background and observation error covariance matrices as in [34,60]. The S1 SSM observations for the three regions were assimilated on a 6-day basis, while the LAI observations from PROBA-V were assimilated on a 10-day basis. The LAI observations were interpolated to the ISBA 1/100° model grid. While the LAI observations were assimilated directly, the S1 SSM was first rescaled to the model climatology before assimilation, following [32,34]. An open-loop (OL) simulation (model run without assimilation) and the analysis were then performed for each region after initialization of the land surface variables. In this study, the LDAS-Monde system used a 24 h window starting at 18:00 UTC and ending at 18:00 UTC the following day, which corresponds to the available hours of S1 SSM products. The assimilation values from the previous window formed the initial conditions for the next 24 h window, allowing fixed estimates of background errors to be used instead of calculating them at the beginning of each cycle. In order to run ISBA-A-gs in offline mode, several surface atmospheric variables are required. In this work, for each day, we used hourly forecast data from AROME-France initiated at 00:00 UTC interpolated on a regular Cartesian grid with a spatial resolution of 1/40° (about 2.5 km at 45°N) made available to the public through the Meteo-France BDAP database (Base de Données Analysées et Prévues). The following atmospheric inputs were used: air temperature, specific humidity, wind speed, and pressure at the lowest vertical level (10 m above canopy), as well as incoming fluxes of shortwave and longwave radiation and liquid and solid (snow) precipitation. The atmospheric data obtained at 1/40° were then reinterpolated at 1/100° with a bi-linear interpolation over the spatial domains involved in this study. To achieve an equilibrium state of ISBA-A-gs and generate more realistic initial conditions, the first year of the study period (2017) was spun up 20 times.

Table 1. Numerical experiments performed in this study for the period 2017 to 2019. All experiments used the same ISBA model version (including multi-layer soil, photosynthesis, and interactive vegetation) and the same AROME-France atmospheric forcing at 1/40°, re-interpolated at 1/100°.

Experiment	Assimilated Observations	Model Equivalent	Control Variables
OL	n/a	n/a	n/a
SSM	S1 SSM (rescaled)	WG2 (1–4 cm)	LAI, WG2 to WG8 (0.01–1 m)
LAI	PROBA-V LAI	LAI	LAI, WG2 to WG8 (0.01–1 m)
SSM and LAI	S1 SSM (rescaled) and PROBA-V LAI	WG2 (1–4 cm), LAI	LAI, WG2 to WG8 (0.01–1 m)

n/a stands for not applicable.

3.2. Evaluation

The primary statistical value used in this study to compare in situ soil moisture observations with satellite estimates was Pearson's correlation coefficient (*R*). In addition to the correlation, the unbiased root mean square difference (ubRMSD), was also used. Its calculation follows:

$$ubRMSD = \sqrt{\frac{\sum_{i=1}^{n}\left[\left(Obs_i - \overline{Obs}\right) - \left(Sat_i - \overline{Sat}\right)\right]^2}{n}}, \tag{1}$$

where *n* represents the number of observations of a given ground station used to validate the satellite retrievals and *Obs* and *Sat* stand for in situ observations and satellite retrievals, respectively. The ubRMSD is used to measure the accuracy of the satellite products. The squared ubRMSD is the difference between the squared RMSD and the squared mean

bias (MB). Since OL simulations are independent from the S1 SSM, they were also used in the evaluation.

Monthly anomalies of modeled RZSM (WG5) were used to evaluate the ability of the model to represent the interannual variability for each experiment:

$$y_{i,j,ref} = \frac{\overline{x}_{i,j} - \overline{x}_{i,ref}}{\overline{x}_{i,ref}} \tag{2}$$

where $y_{i,j,ref}$ is the relative mean difference value for a given experiment output at the grid point where the ground station is located for the ith month and the jth year with respect to a reference (*ref*) year. The first year of the time series (2017) was used as the reference year. The same procedure was applied to the in situ soil moisture measurements at a depth of 0.3 m.

The assimilation of S1, SSM, and LAI, was first evaluated at the local scale using in situ RZSM observations. The comparison of in situ and simulated RZSM seasonal cycles can be affected by confounding factors, such as representativeness errors, and preliminary tests showed that the assimilation had little effect on the results derived from a direct comparison of RZSM time series. Instead, we investigated the ability of the assimilation to improve the representation of interannual variability using Equation (2).

In a second step, a regional comparison of the simulated RZSM was made for contrasting soil moisture conditions, with the aim of quantifying the effect of the assimilation.

4. Results

4.1. Validation of S1 SSM

Validation of the 1 km × 1 km S1 SSM products was first carried out by conducting a comparison with in situ SSM observations obtained from the SMOSMANIA, Meteopole-Flux, and REMEDHUS stations located within the study regions, as shown in Figure 1. A time series of daily SSM values at 5 cm depth, at 18:00 UTC, is presented in Figure 5, for the La Grand Combe (LGC) SMOSMANIA station located within the Montpellier domain (see Figure 2 for LGC location within the domain). Figure 5 also shows the S1 SSM values corresponding to the pixel where this in situ station is located, together with the OL simulation. The S1 SSM product matches the seasonal variability of the observed SSM, with better agreement in wetter conditions compared to drier ones. The observed values range between 0.005 and 0.26 m³ m⁻³, while the satellite product varies from 0.07 to 0.20 m³ m⁻³. Notably, S1 SSM represents some of the peak SSM values quite well, especially in November and December 2017. Table 2 shows that S1 SSM tended to perform better than the OL simulation over LGC, for all values. S1 SSM had an ubRMSD of 0.024 m³ m⁻³, against 0.058 m³ m⁻³ for the OL simulation. On the other hand, OL WG2 correlated slightly better with in situ SSM observations than S1 SSM.
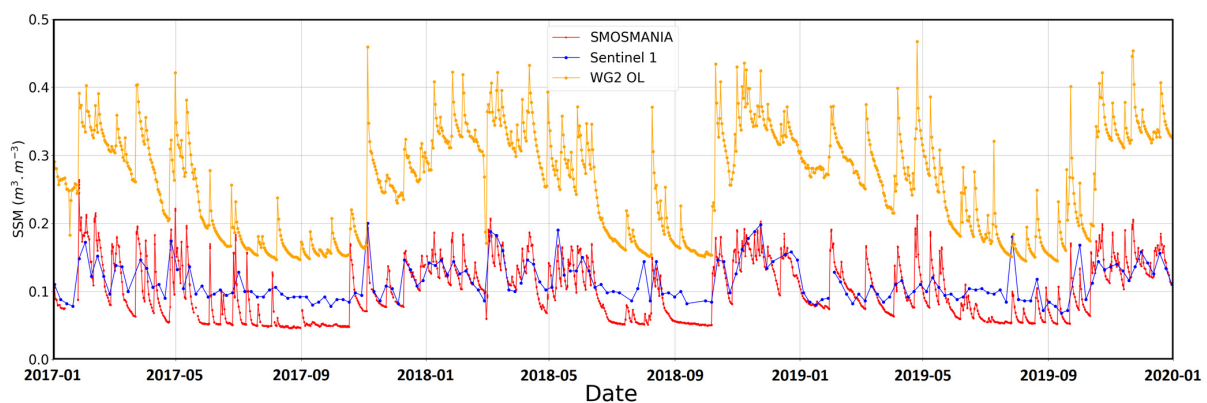

Figure 5. Hourly time series of surface soil moisture at the LGC station from in situ measurements, S1 SSM, and OL WG2 simulations (red, blue, and orange lines, respectively) at 18:00 UTC.

Table 2. Correlation coefficient (*R*), root mean square difference (RMSD), unbiased RMSD (ubRMSD), and mean bias (MB) between OL simulations, S1 SSM products, and in situ observations at the LGC SMOSMANIA station, from 2017 to 2019, at 18:00 UTC.

Comparison	*R*	ubRMSD (m³ m⁻³)	RMSD (m³ m⁻³)	MB (m³ m⁻³)	Number
OL vs. in situ	0.87	0.043	0.165	0.159	165
S1 SSM vs. in situ	0.85	0.024	0.028	−0.013	163
S1 SSM vs. OL	0.71	0.058	0.156	−0.145	164

To better assess the accuracy of the S1 SSM product, a seasonal statistical analysis was performed to compare it with the observed SSM at LGC. The scatter plots and correlation coefficients between the two datasets for each season are presented in Figure 6, with winter, spring, and fall showing high correlation coefficient values (*R* = 0.92, 0.88, and 0.91, respectively). Overall, a good correlation was observed between the datasets for all seasons, except for summer, for which the lowest correlation coefficient was obtained (*R* = 0.62).
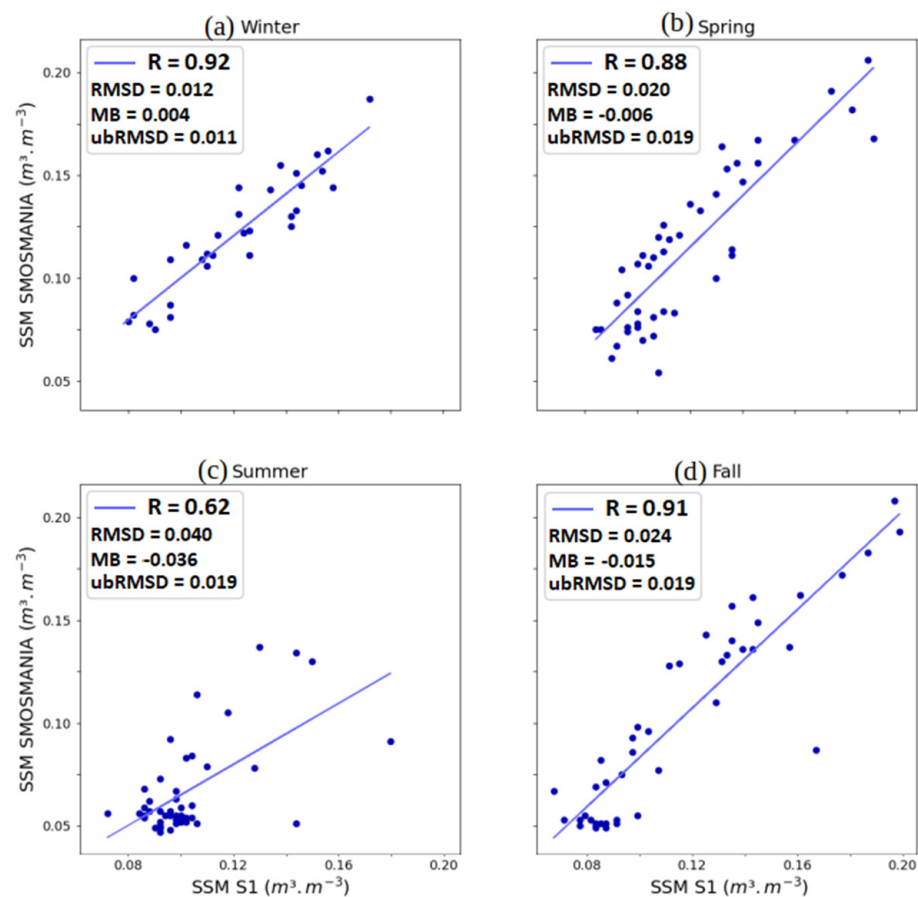

Figure 6. SMOSMANIA versus S1 SSM products for the LGC station for (**a**) winter (December, January, and February), (**b**) spring (March, April, and May), (**c**) summer (June, July, and August), and (**d**) fall (September, October, and November), at 18:00 UTC. The best linear fit as well as the correlation coefficient between the two datasets are presented in each sub-plot. RMSD, MB, and ubRMSD values are in m³m⁻³. Freezing cases were sorted out by excluding data for which soil temperature at 5 cm depth was below 4 °C.

The statistical distribution of the correlation coefficients between the S1 SSM products and the observed SSM is shown in Figure S1 for all seasons and over the three years, for all SMOSMANIA (Toulouse and Montpellier Regions) and REMEDHUS (Salamanca Region) stations. A seasonal variation of *R* can be observed across stations for all regions. A lower

correlation between the satellite products and the observed SSM was obtained during the summer season, which supports the results presented in Figure 5 for this season. In general, SMOSMANIA stations showed higher correlation coefficients than REMEDHUS, especially in spring and fall. However, one of the SMOSMANIA stations (LHS) showed a negative correlation in summer. The correlation values showed greater variability over the four seasons in the Salamanca region, which is partly due to the higher number of stations in this region. In addition, some of the stations in Salamanca showed no correlation between observed and satellite-derived SSM products. These stations are located in an agricultural area where irrigation may be used. One consequence of irrigation is that the SSM increases regardless of precipitation events. The S1 SSM may be sensitive to irrigation, while in situ observations are not affected by irrigation.

Considering the entire study period (see "All" box plots in Figure S1), a good agreement was observed for SMOSMANIA and REMEDHUS, with mean correlation coefficients of 0.63 and 0.51, respectively. This indicates that S1 SSM is able to capture the characteristics of in situ measurements. When the analysis was performed for the S1 SSM products at 06:00 UTC, the statistics between these products and the in situ measurements showed a reduced accuracy.

The correlation coefficient and unbiased root mean square difference (ubRMSD, Equation (1)) values between the SMOSMANIA, Meteopole-Flux, and REMEDHUS stations and the S1 SSM products for the whole study period are listed in the Supplementary Materials (Table S1). It is shown that good correlation coefficients were obtained for most of the stations (F-test p-value < 0.01), with the exception of Las Brozas in the Salamanca region, which showed a poor value of 0.09 and a p-value = 0.1. For all the other stations, p-values lower than 0.01 were obtained, indicating that the correlation was significant. Regarding the ubRMSD, typical values ranging from 0.030 to 0.120 $m^3 \, m^{-3}$ were found for all stations. The availability of S1 SSM products is better for Salamanca than for the two regions in France, leading to a larger number of observations for Salamanca, ranging from 180 to 361. Note that a better correlation of OL WG2 with in situ SSM observations was systematically observed for all stations (Table S2). Among the 26 stations considered in Table S2, OL WG2 R-values less than 0.6 were observed for only 4 REMEDHUS stations: El Coto, Las Brozas, Las Tres Rayas, and Las Victorias (R = 0.44, 0.54, 0.59, and 0.58, respectively). S1 SSM presented smaller ubRMSD values than OL WG2 for only six stations: LGC, Carretoro, El Coto, El Tomillar, Las Victorias, and Paredinas.

4.2. Assimilation

The effect of the assimilation was shown for the Montpellier region. In this region, the summer of 2019 experienced a pronounced drought [61], while the summer of 2018 was relatively wet and the summer of 2017 was moderately dry [62]. When using Equation (2), 2017 was used as the reference year. The effect of the assimilation on the simulated RZSM was more apparent when contrasting years, such as 2018 and 2019, were considered.

4.2.1. Local Comparison

Following the validation of the S1 SSM products against in situ measurements, the influence of assimilating the S1 SSM products alone, together with LAI, and assimilating LAI alone on the simulated 0.01–0.04 m SSM and 0.2–0.4 m RZSM (WG2 and WG5, respectively) was investigated.

The impact of the assimilation was first evaluated on WG2 for the three assimilation experiments by comparing them with the OL outputs for the three study regions. Very little or no impact on the simulated WG2 was found (with respect to the score values presented in Table S2). A larger impact of assimilation was observed on WG5. To better visualize the impact of the assimilation experiments on WG5, a relative local mean value was calculated for each analysis as well as for the in situ measurements for each of the stations in the Montpellier region using Equation (2).

Figure 7 illustrates the relationship between the relative mean local interannual differences (Equation (2)) of the observed RZSM from SMOSMANIA and those from the OL and analysis simulations for the Montpellier region. In 2018, the in situ measurements showed wetter conditions compared to 2017, as the relative differences were greater than 0, while 2019 was drier. The interannual variability was well represented in both the model and the analysis at the 0.3 m soil depth. There was a difference in scale for the relative differences coming from the model and the in situ measurements. This difference was due to the spatial and temporal resolution of the two sources of information. The joint assimilation of SSM and LAI satellite products led to a slightly better correlation with respect to the OL (*R* = 0.70 and 0.66, respectively). The values of the RMSD and the MB scores were improved.
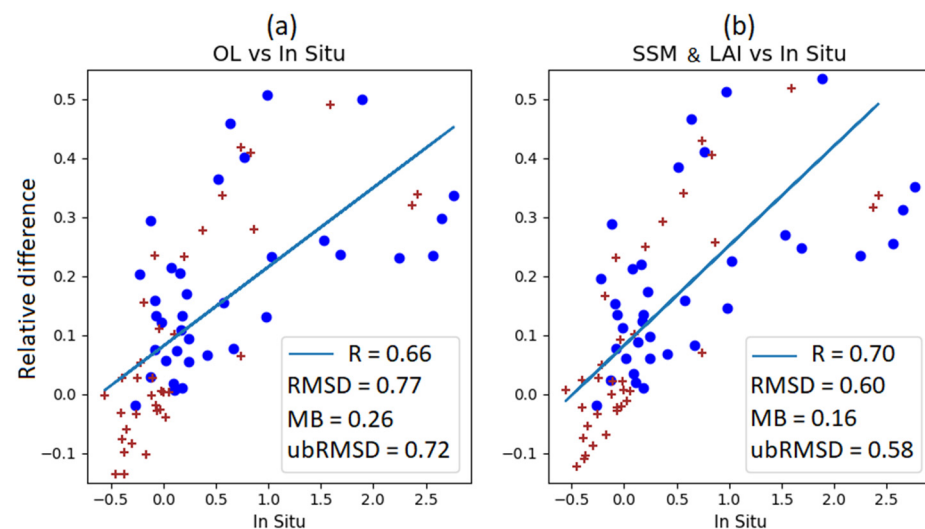

Figure 7. Monthly (January to December) mean relative difference values of the observed soil moisture at 0.30 m soil depth vs. (**a**) open-loop WG5 simulations and (**b**) analyzed WG5 from the joint assimilation of SSM and LAI for the three SMOSMANIA stations of the Montpellier region. The year of reference to estimate these relative values was 2017. The 2018 and 2019 relative differences are represented by blue dots and red crosses, respectively.

4.2.2. Regional Comparison

Particular attention was given to the contrasting summers of 2018 and 2019 in the Montpellier region. Figure 8 shows a comparison of the RZSM simulations (WG5) between July 2019 and July 2018. The difference between the averaged open-loop simulations shows that July 2019 was mostly dryer than July 2018, with certain areas showing a more pronounced difference, especially in the northwest, where some CFs are located (Figure 3). Figure 9 shows the annual evolution from 2018 to 2019 of the mean differences in July between the analyzed WG5 and the OL WG5 simulations. The red (blue) color indicates that the analysis added (removed) more water to the root zone in 2019 than in 2018. The S1 SSM assimilation had little effect on this year-to-year WG5 difference, except for a localized increase in added water in the Alès cropland area sub-domain (box in Figure 9) in the northeast of the domain. In contrast, the assimilation of LAI had a much greater impact on the changes in WG5, with a tendency to increase WG5 more in 2019 in most of the region, especially in the southeastern part. When S1 SSM and LAI were assimilated together (Figure 9c), the impact appeared to be similar to that when LAI was assimilated alone, but it was amplified in the cropland area in the northeast of the domain. Note that Figure 9c corresponds to the difference between Figure 8a,b.
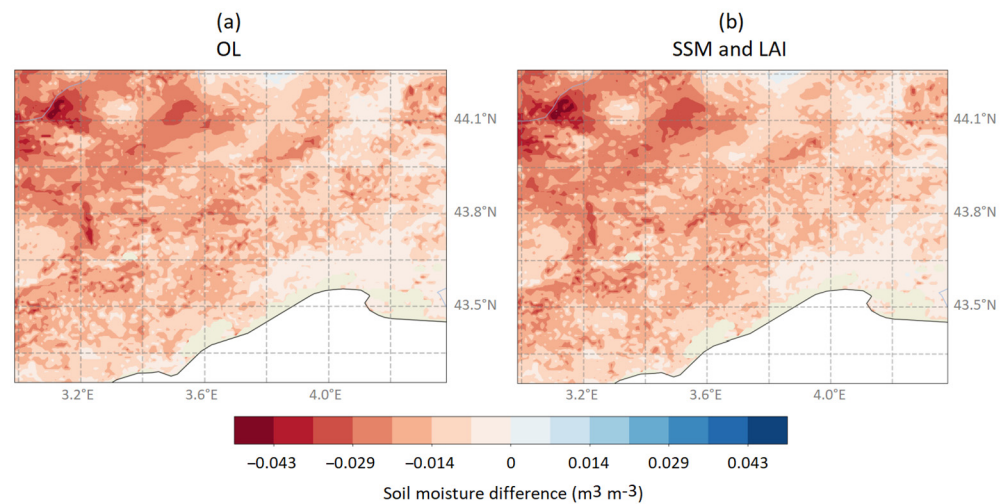
Figure 8. Map over the Montpellier domain of the WG5 difference between the averaged values of July 2019 and July 2018 from (**a**) the open-loop and (**b**) the joint assimilation of SSM and LAI.
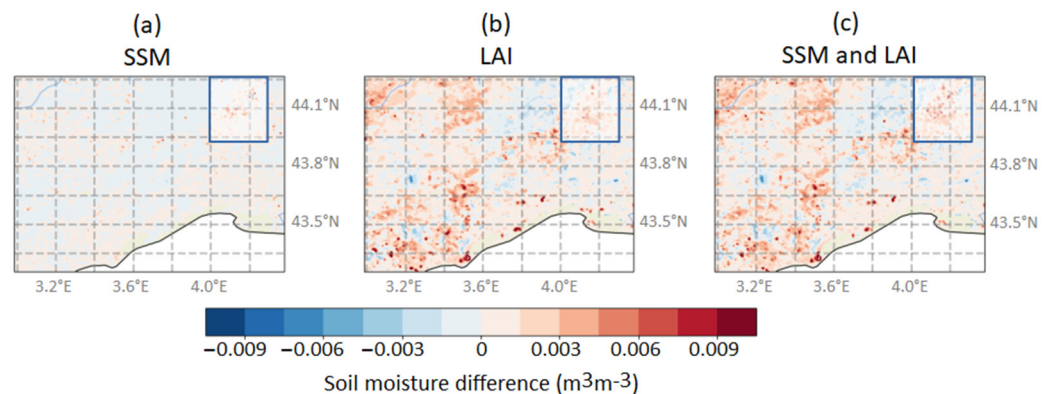

Figure 9. Year-to-year evolution from 2018 to 2019 over the Montpellier domain of the mean differences in July between analyzed and open-loop WG5 when (**a**) S1 SSM was assimilated alone, (**b**) PROBA-V LAI was assimilated alone, and (**c**) S1 SSM and PROBA-V LAI were jointly assimilated. Boxes correspond to the Alès sub-domain area shown in Figures 3 and 10. Figure 9c corresponds to the difference between Figure 8a,b. The red (blue) color indicates that the analysis added (removed) water to the root zone more in 2019 than in 2018 in response to the assimilation.

To further investigate the impact of assimilation, a closer examination of the Alès subdomain, marked by blue rectangles in Figure 9 (4–4.3°E, 43.95–44.25°N), was performed and is shown in Figure 10. Figure 10 includes the irrigation zones obtained from Meier et al. [51] at kilometer resolution for this region. Figure 10 shows that the impact of assimilation varied between different analyses and that the assimilation of S1 SSM alone resulted in moderate changes in the July 2019 WG5 analysis in some areas compared to July 2018. The impact of LAI assimilation on WG5 was more pronounced and different when LAI was jointly assimilated together with S1 SSM. Figure 10 also shows that LAI was reduced by the assimilation. Similar results were obtained over the Toulouse and Salamanca regions (see the Supplementary Materials).
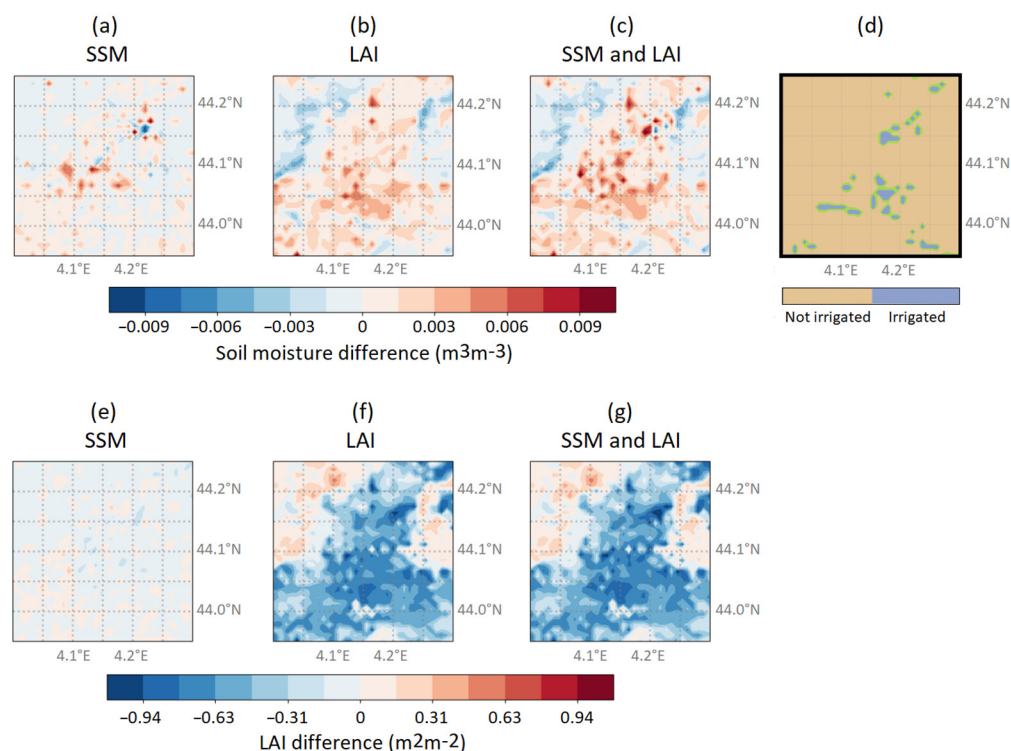
Figure 10. Year-to-year evolution from 2018 to 2019 over the Alès sub-domain of the mean differences in July between (**a**–**c**) analyzed and open-loop WG5 and (**e**–**g**) LAI, when (**a**,**e**) S1 SSM was assimilated alone, (**b**,**f**) PROBA-V LAI was assimilated alone, and (**c**,**g**) SSM and LAI were jointly assimilated, compared with (**d**) the spatial distribution of irrigation from Meier et al. [51]. The red (blue) color indicates that the analysis added (removed) water to the root zone and increased (decreased) LAI more in 2019 than in 2018 in response to the assimilation.

5. Discussion

5.1. Does S1 SSM Perform Better than Other SSM Products?

The results in Table S1 are consistent with similar studies comparing satellite-derived products with ground-based measurements (e.g., [63–67]). Table 3 summarizes the S1 SSM validation results of this study and compares them with results from El Hajj et al. [66] and Portal et al. [67]. The latter results include Advanced Scatterometer (ASCAT), Soil Moisture Active and Passive (SMAP), Soil Moisture and Ocean Salinity (SMOS), and SMOS INRAE-CESBIO (SMOS-IC) products.

The station-averaged R and ubRMSD values we obtained over Southern France, 0.60 and 0.062 m^3 m^{-3}, respectively, are consistent with the results of El Hajj et al. [66] for S1 SSM products at 1 km resolution over this area (0.59 and 0.056 m^3 m^{-3}, respectively). A key finding of El Hajj et al. [66] is that the values of these scores are not much affected by spatial resolution, for spatial resolutions ranging from 1 km to 25 km. For the Salamanca region, the S1 SSM R score was not as good, R = 0.48, but the accuracy was similar, with a ubRMSD value of 0.053 m^3 m^{-3}. The lower score may be due to the fact that some REMEDHUS stations are irrigated from time to time, as reported by ISMN (https://ismn.earth/en/news/, accessed on 30 August 2023), or that irrigation is dominant in the 1 km × 1 km grid cell while absent over the station. A temporal discontinuity in the in situ SSM was observed during the summer of 2018, triggering a decrease in SSM values. Visual inspection of the Google map image covering the Las Brozas station and of the soil moisture observations from this station showed that surface runoff from a nearby irrigated field can occur. Portal et al. [67] used only selected REMEDHUS stations.

Table 3. Comparison of the performance of S1 SSM with other satellite SSM products over Southern France and the Salamanca region. Average correlation coefficient (*R*), unbiased root mean square difference (ubRMSD), and number of locations are indicated. El Hajj et al. [66] used SMOSMANIA stations together with additional soil moisture measurements in the region of Montpellier.

SSM Product, Spatial Resolution, Reference	Region, Soil Moisture Network, Period	Average *R*	Average ubRMSD $(m^3\ m^{-3})$	Number of Stations
S1, 1 km, this study	Toulouse, SMOSMANIA, 2017–2019	0.57	0.072	4
S1, 1 km, this study	Montpellier, SMOSMANIA, 2017–2019	0.64	0.05	3
S1, 1 km, this study	Salamanca, REMEDHUS, 2017–2019	0.48	0.053	19
S1, 1 km, [66]	Southern France (SMOSMANIA and Montpellier), 2016–2017	0.59	0.056	8
SMAP-S1, 1 km, [66]	Southern France (SMOSMANIA and Montpellier), 2016–2017	0.48	0.043	8
SMAP-S1, 1 km, [67]	Salamanca, REMEDHUS (rainfed crops only), 2015–2017	0.86	0.04	7
ASCAT, 25 km, [66]	Southern France (SMOSMANIA and Montpellier), 2016–2017	0.49	0.062	8
SMOS-IC, 25 km, [66]	Southern France (SMOSMANIA and Montpellier), 2016–2017	0.57	0.053	8
SMOS, 25 km, [67]	Salamanca, REMEDHUS, 2015–2017	0.65	0.062	6
SMAP, 36 km, [66]	Southern France (SMOSMANIA and Montpellier), 2016–2017	0.69	0.047	8
SMAP, 36 km, [67]	Salamanca, REMEDHUS, 2015–2017	0.7	0.058	6

5.2. Why Is a Synergy of S1 SSM with LAI Observed in the Assimilation?

Previous results based only on the assimilation of low-resolution SSM products have shown that the assimilation of SSM in ISBA has a limited impact on RZSM. The LAI assimilation has a much larger impact. The reason for this is that the sensitivity of SSM to small perturbations in the model soil moisture profile is greatly reduced below the depth of 0.1 m, while the sensitivity of LAI peaks for the 0.2–0.4 m soil layer, i.e., for WG5 [34,68]. Under dry conditions, RZSM is somewhat decoupled from SSM [69], but not from LAI. Figures 9 and 10 show that the assimilation of S1 SSM alone can induce limited changes in RZSM and in LAI and that these changes vary from place to place. However, the assimilation of SSM products alone is not sufficient to significantly improve ISBA outputs. Errors in the ISBA soil and vegetation parameters, land cover, and topography affect the SSM simulations. The impact of SSM products alone is reduced by the use of the seasonal linear rescaling applied to the assimilated product, which results in the loss of part of the original information contained in the SSM product. Therefore, the assimilation of SSM products must be combined with other relevant satellite-based products, such as LAI, to improve the accuracy of LSM outputs. It was checked that this conclusion is valid for all seasons. The larger impact of the joint assimilation of S1 SSM and LAI products can be explained by (1) the direct link of S1 SSM with soil moisture of the more superficial soil layers, (2) the indirect effect of LAI on SSM and RZSM through its influence on evapotranspiration, (3) the indirect effect of SSM on LAI, and (4) the direct effect of LAI assimilation on RZSM. This finding is consistent with previous studies (e.g., [8,70]) and confirms the importance of considering these two variables to disentangle the complex land–atmosphere interactions. Most of the areas with positive LAI differences in response to the assimilation (Figure 10g,f) correspond to closed forests, as seen in Figure 3. Over urban areas, these differences are very small. Conversely, other areas showed a decrease in simulated LAI in response to assimilation. Negative LAI changes were mostly observed over agricultural areas.

Figure 11 shows the relationship between the LAI differences and WG5 differences displayed in Figure 10 for the three experiments. When SSM was assimilated alone, no clear relationship between the LAI differences and WG5 differences was observed, but increases in WG5 in July 2019 with respect to July 2018 tended to trigger an increase in LAI (*R* = 0.22).

When LAI was assimilated alone, changes in LAI were negatively correlated with changes in WG5 ($R = -0.82$). This can be explained by the reduced evapotranspiration caused by lower LAI values. The addition of S1 SSM in the assimilation changed this relationship in the agricultural areas, with a greater variety of WG5 difference values, either negative or positive. The largest WG5 differences could be related to increased irrigation during summer 2019 to counteract the drought that occurred. The irrigation map in Figure 10d presents similarities with the increased addition of water. However, detecting irrigation from S1 data is challenging [71,72] because (1) the C-band signal from the soil is attenuated by well-developed vegetation and (2) the S1 sampling time is not sufficient. Moreover, errors in the land cover map used in the retrieval process may propagate to the SSM values, especially in heterogeneous landscapes.
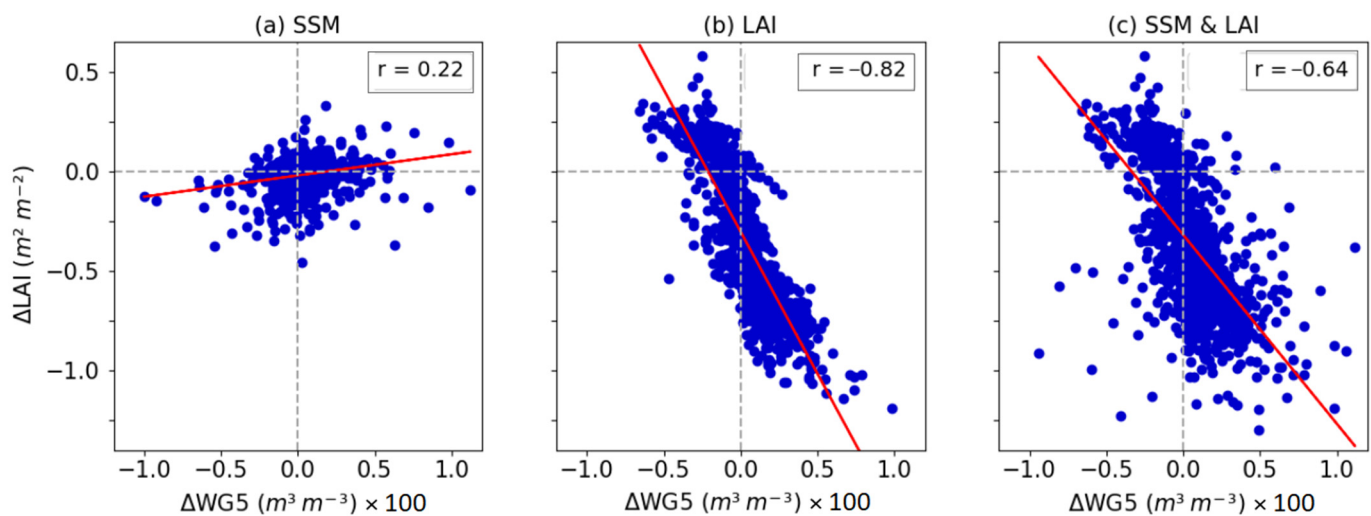
Figure 11. Year-to-year evolution from 2018 to 2019 over the Alès sub-domain of the mean differences in July between analyzed and open-loop LAI vs. the mean differences in July between analyzed and open-loop WG5 between (**a**) S1 SSM assimilated alone, (**b**) PROBA-V LAI assimilated alone, and (**c**) SSM and LAI jointly assimilated.

5.3. Can Geology and Land Use Affect the Assimilation?

Land use is a critical factor that can significantly affect the accuracy of satellite product assimilation in land surface models [56]. The accuracy of assimilation results largely depends on the similarity between land surface characteristics, satellite observations, and the land cover database used in LSMs. Several studies have investigated the influence of land use on the assimilation of satellite products in LSMs. For example, Draper et al. [73] found that the accuracy of soil moisture assimilation was higher in cropland than that in forested areas due to the higher sensitivity of the radar signal to soil moisture in cropland. In this study, the ECOCLIMAP-II land cover map was used in the model simulations, which differs slightly from the CGLS-LC100 map shown in Figure 3. The LAI—and indirectly SSM—contributions in this specific case could be related to the percentage of forest present in these areas in the ECOCLIMAP-II database, which is less than 50%, indicating the use of other land uses in the ISBA model.

The Montpellier region is characterized as a very contrasted area in terms of land use, as shown in Figure 3. The size of the Alès sub-domain ($0.3° \times 0.3°$) would correspond to the size of a low-resolution SSM pixel. Figure 10 illustrates the large sub-pixel variability that would be lost at low spatial resolution. Another characteristic of the Montpellier region is the presence of karst areas in the northwest of the domain (Larzac and Cévennes) and flood irrigation for rice production in the southeast of the domain (Camargue). Karstic areas tend to trigger anomalous C-band backscatter signals [74,75], and irrigation is not represented by the ISBA model version we used. In Section 4.1, it was shown that the OL

WG2 tends to perform better than the S1 SSM, with better *R* and ubRMSD score values. Therefore, we can use OL WG2 as a benchmark for S1 SSM over non-irrigated areas (OL does not represent irrigation). Figure 12 shows S1 SSM vs. OL WG2 *R* and ubRMSD maps showing specific problems with the S1 SSM over the karst areas. These maps also show a discrepancy between OL and S1 over the flood-irrigated Camargue area caused by the non-implementation of irrigation in the model version we used. Figure 12c,d also shows the impact of the joint assimilation of S1 SSM and LAI ("SSM and LAI" experiment in Table 2) on the *R* and ubRMSD score values.
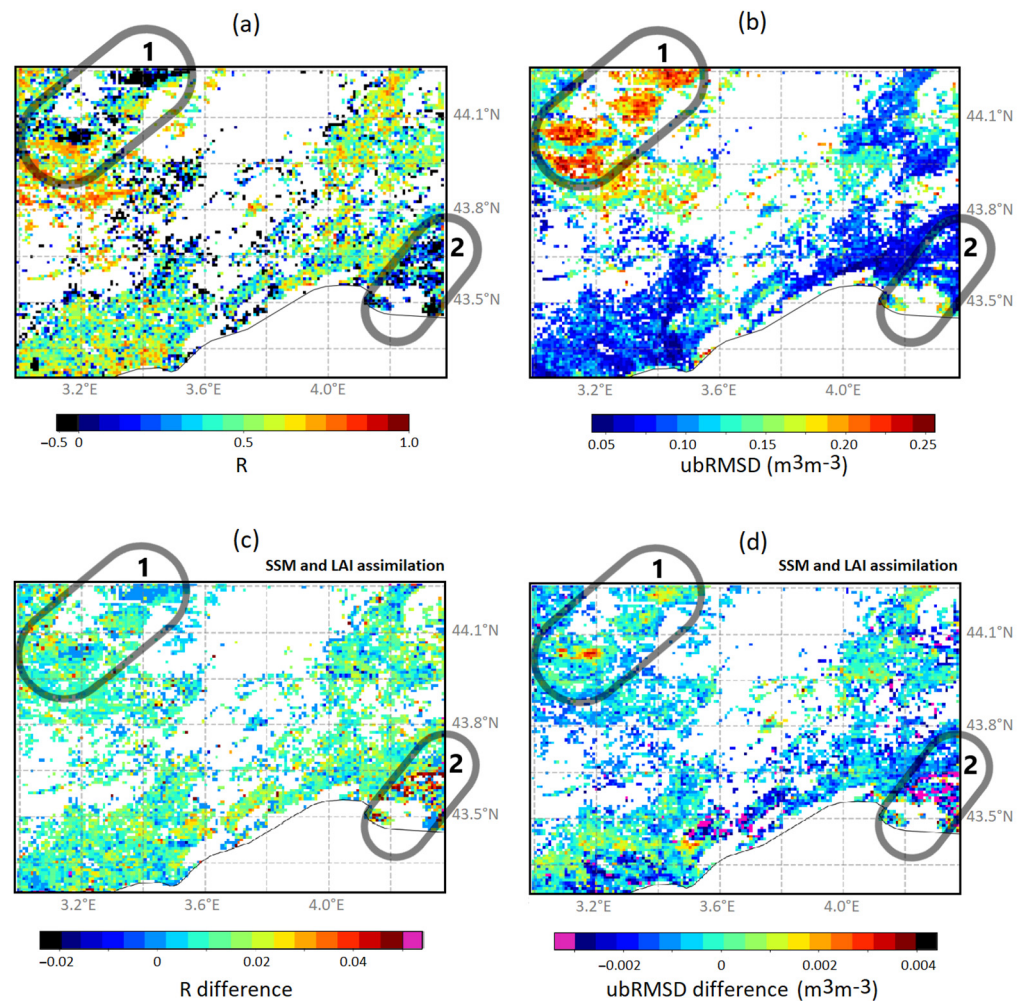
Figure 12. S1 SSM vs. OL WG2 over the Montpellier domain: (**a**) correlation coefficient, (**b**) ubRMSE, (**c**) difference between correlation of S1 SSM vs. SSM and LAI analysis WG2 and correlation of S1 SSM vs. OL WG2, and (**d**) difference between ubRMSD of S1 SSM vs. SSM and LAI analysis WG2 and ubRMSD of S1 SSM vs. OL WG2. The karst area of Larzac and Cevennes and the flood irrigated area of Camargue are shown ("1" and "2", respectively).

Overall, the assimilation had a neutral or negative effect on *R* and ubRMSD over the karst area. On the other hand, over the Camargue, the consistency between the S1 SSM and the modeled WG2 was improved by the assimilation, with an increase in *R* (up to 0.05) and a decrease in ubRMSD (down to −0.003). This shows that the assimilation is able to correct the model deficiencies to some extent. To evaluate the difference of the analysis with respect to the OL, with and without assimilation of S1 SSM and PROBA-V LAI, Figure 13 presents the equivalent of Figure 12c,d for the "SSM" and "LAI" experiments (Figure 13a,b and Figure 13c,d, respectively). As far as the correlation difference is concerned, it seems that Figure 12c is more similar to Figure 13a ("SSM") than to Figure 13c ("LAI"). The opposite

can be observed for the ubRMSD difference, Figure 12d having more similarities with Figure 13d ("LAI") than with Figure 13b ("SSM"). Over the Camargue, the improvement in consistency between the S1 SSM and the modeled WG2 was limited to a few grid cells in the "LAI" and "SSM" experiments. The more extensive improvement obtained with the "SSM and LAI" experiment over the Camargue demonstrates the synergy between S1 SSM and LAI observations in the assimilation over intensively irrigated areas.
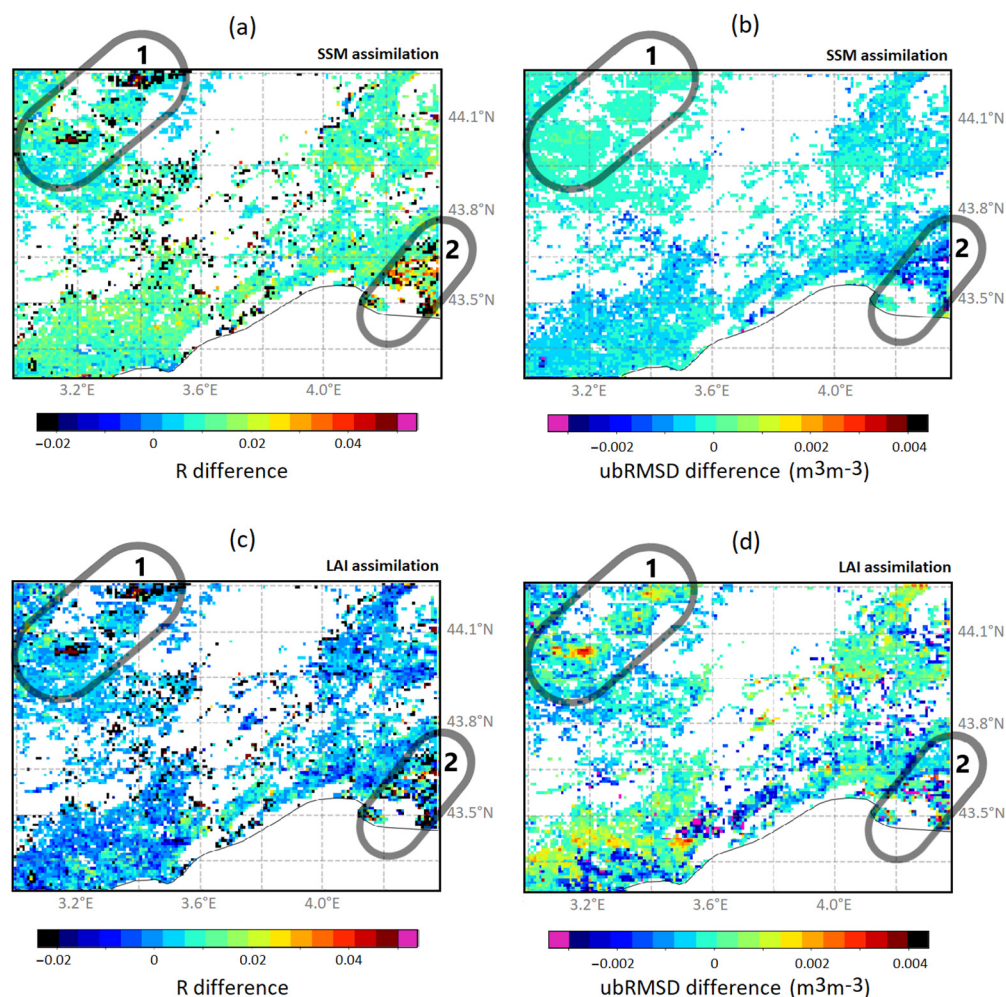

Figure 13. Impact of SSM assimilation alone (**a,b**) and LAI assimilation alone (**c,d**): (**a,c**) difference between correlation of S1 SSM vs. SSM and LAI analysis WG2 and correlation of S1 SSM vs. OL WG2; (**b,d**) difference between ubRMSD of S1 SSM vs. SSM and LAI analysis WG2 and ubRMSD of S1 SSM vs. OL WG2. The karst area of Larzac and Cevennes and the flood irrigated area of Camargue are shown ("1" and "2", respectively).

For the other two regions, the same study case as for Montpellier was performed for July 2018 and July 2019. For the Toulouse region, July 2019 was also drier than July 2018. As for Montpellier, the assimilation of S1 SSM alone did not have much impact on WG5. The assimilation of LAI and LAI together with S1 SSM had more impact with respect to OL, especially in agricultural areas. This can be explained by a possible irrigation relationship, as observed in the Montpellier region, and more accurate S1 SSM retrievals in agricultural areas [71]. Similar results were observed over Salamanca. Assimilation results for Toulouse and Salamanca regions can be found in the Supplementary Materials of this paper.

6. Conclusions

This study investigated the benefits of assimilating satellite-derived soil moisture (SSM) products from the Sentinel-1 (S1) satellite in the ISBA land surface model at a spatial resolution of 1 km, from 2017 to 2019, using the LDAS-Monde tool, for two regions in Southern France and one in Spain. The validation of the S1 SSM was carried out by comparing it with in situ measurements of soil moisture at a depth of 5 cm from the SMOSMANIA network and Meteopole-Flux in France and the REMEDHUS network in Spain. The results showed a good agreement between the two datasets for most of the stations at 18:00 UTC, with some difficulties during summer due to irrigation processes in Spain, as the REMEDHUS stations are located in semi-arid croplands. The SSM simulations were generally more precise than the S1 SSM observations, and the ISBA simulations could be used together with in situ observations to validate the S1 SSM. Three different experiments were carried out to study the influence of the assimilation of S1 SSM and PROBA-V LAI, alone and together, on the simulated soil moisture at the 0.01–0.04 m (WG2) and 0.20–0.40 m (WG5) soil layers. It was shown that the S1 SSM assimilation alone had little effect on the soil moisture at both depths, across all seasons. In contrast, there was a more pronounced effect on soil moisture in the root zone (WG5) for the other two experiments. Over agricultural areas, the effect of the three experiments on WG5 differed, and the assimilation of S1 SSM had a greater impact on the analysis results. Similar results were observed for the three regions considered in this study. Since the impact of S1 SSM was particularly visible over agricultural areas, this shows that S1 SSM observations can help to detect and monitor drought impacts on agriculture. The observed synergies between S1 SSM and satellite-derived LAI suggest that high-resolution SSM products have added value in a data assimilation context. This was particularly true over irrigated areas, as irrigation was not represented in the ISBA simulations. This finding contrasts with previous results based on low-resolution SSM products. Future work will focus on the assimilation of S1 backscatter, as it provides information from both SSM and LAI [12].

References

1. Bartalis, Z.; Wagner, W.; Naeimi, V.; Hasenauer, S.; Scipal, K.; Bonekamp, H.; Figa, J.; Anderson, C. Initial Soil Moisture Retrievals from the METOP-A Advanced Scatterometer (ASCAT). *Geophys. Res. Lett.* **2007**, *34*, L20401. [CrossRef]
2. Kerr, Y.H.; Waldteufel, P.; Wigneron, J.-P.; Delwart, S.; Cabot, F.; Boutin, J.; Escorihuela, M.-J.; Font, J.; Reul, N.; Gruhier, C.; et al. The SMOS mission: New tool for monitoring key elements of the global water cycle. *Proc. IEEE* **2010**, *98*, 666–687. [CrossRef]
3. Massari, C.; Camici, S.; Ciabatta, L.; Brocca, L. Exploiting Satellite-Based Surface Soil Moisture for Flood Forecasting in the Mediterranean Area: State Update Versus Rainfall Correction. *Remote Sens.* **2018**, *10*, 292. [CrossRef]
4. Sehgal, V.; Gaur, N.; Mohanty, B.P. Global Flash Drought Monitoring Using Surface Soil Moisture. *Water Resour. Res.* **2021**, *57*, e2021WR029901. [CrossRef]
5. Seneviratne, S.I.; Corti, T.; Davin, E.L.; Hirschi, M.; Jaeger, E.B.; Lehner, I.; Orlowsky, B.; Teuling, A.J. Investigating Soil Moisture–Climate Interactions in a Changing Climate: A Review. *Earth Sci. Rev.* **2010**, *99*, 125–161. [CrossRef]
6. Martínez-Fernández, J.; González-Zamora, A.; Sánchez, N.; Gumuzzio, A.; Herrero-Jiménez, C.M. Satellite Soil Moisture for Agricultural Drought Monitoring: Assessment of the SMOS Derived Soil Water Deficit Index. *Remote Sens. Environ.* **2016**, *177*, 277–286. [CrossRef]
7. Wagner, W.; Blöschl, G.; Pampaloni, P.; Calvet, J.-C.; Bizzarri, B.; Wigneron, J.-P.; Kerr, Y. Operational Readiness of Microwave Remote Sensing of Soil Moisture for Hydrologic Applications. *Hydrol. Res.* **2007**, *38*, 1–20. [CrossRef]
8. Peng, J.; Albergel, C.; Balenzano, A.; Brocca, L.; Cartus, O.; Cosh, M.H.; Crow, W.T.; Dabrowska-Zielinska, K.; Dadson, S.; Davidson, M.W.J.; et al. A Roadmap for High-Resolution Satellite Soil Moisture Applications—Confronting Product Characteristics with User Requirements. *Remote Sens. Environ.* **2021**, *252*, 112162. [CrossRef]
9. Abbaszadeh, P.; Moradkhani, H.; Zhan, X. Downscaling SMAP radiometer soil moisture over the CONUS using an ensemble learning method. *Water Resour. Res.* **2019**, *55*, 324–344. [CrossRef]
10. El Hajj, M.; Baghdadi, N.; Zribi, M.; Bazzi, H. Synergic Use of Sentinel-1 and Sentinel-2 Images for Operational Soil Moisture Mapping at High Spatial Resolution over Agricultural Areas. *Remote Sens.* **2017**, *9*, 1292. [CrossRef]
11. El Hajj, M.; Baghdadi, N.; Wigneron, J.-P.; Zribi, M.; Albergel, C.; Calvet, J.-C.; Fayad, I. First Vegetation Optical Depth Mapping from Sentinel-1 C-band SAR Data over Crop Fields. *Remote Sens.* **2019**, *11*, 2769. [CrossRef]
12. Foucras, M.; Zribi, M.; Albergel, C.; Baghdadi, N.; Calvet, J.-C.; Pellarin, T. Estimating 500-m Resolution Soil Moisture Using Sentinel-1 and Optical Data Synergy. *Water* **2020**, *12*, 866. [CrossRef]
13. Madelon, R.; Rodríguez-Fernández, N.J.; Bazzi, H.; Baghdadi, N.; Albergel, C.; Dorigo, W.; Zribi, M. Soil moisture estimates at 1 km resolution making a synergistic use of Sentinel data. *Hydrol. Earth Syst. Sci.* **2023**, *27*, 1221–1242. [CrossRef]
14. Dirmeyer, P.A.; Gao, X.; Zhao, M.; Guo, Z.; Oki, T.; Hanasaki, N. The Second Global Soil Wetness Project (GSWP-2): Multi-model analysis and implications for our perception of the land surface. *Bull. Am. Meteorol. Soc.* **2006**, *87*, 1381–1397. [CrossRef]
15. Schellekens, J.; Dutra, E.; Martínez-de la Torre, A.; Balsamo, G.; van Dijk, A.; Sperna Weiland, F.; Minvielle, M.; Calvet, J.-C.; Decharme, B.; Eisner, S.; et al. A global water resources ensemble of hydrological models: The eartH2Observe Tier-1 dataset, *Earth Syst. Sci. Data* **2017**, *9*, 389–413. [CrossRef]
16. Noilhan, J.; Mahfouf, J.-F. The ISBA Land Surface Parameterisation Scheme. *Global Planet. Chang.* **1996**, *13*, 145–159. [CrossRef]
17. Calvet, J.-C.; Noilhan, J.; Roujean, J.-L.; Bessemoulin, P.; Cabelguenne, M.; Olioso, A.; Wigneron, J.-P. An Interactive Vegetation SVAT Model Tested against Data from Six Contrasting Sites. *Agric. For. Meteorol.* **1998**, *92*, 73–95. [CrossRef]
18. Calvet, J.-C.; Rivalland, V.; Picon-Cochard, C.; Guehl, J.-M. Modelling forest transpiration and CO_2 fluxes—Response to soil moisture stress. *Agric. For. Meteorol.* **2004**, *124*, 143–156. [CrossRef]
19. Gibelin, A.-L.; Calvet, J.-C.; Roujean, J.-L.; Jarlan, L.; Los, S.O. Ability of the land surface model ISBA-A-gs to simulate leaf area index at the global scale: Comparison with satellites products. *J. Geophys. Res.* **2006**, *111*, D18102. [CrossRef]
20. Albergel, C.; Rüdiger, C.; Pellarin, T.; Calvet, J.-C.; Fritz, N.; Froissard, F.; Suquia, D.; Petitpa, A.; Piguet, B.; Martin, E. From near-surface to root-zone soil moisture using an exponential filter: An assessment of the method based on in-situ observations and model simulations. *Hydrol. Earth Syst. Sci.* **2008**, *12*, 1323–1337. [CrossRef]
21. Meng, X.; Wang, H.; Chen, J.; Yang, M.; Pan, Z. High-Resolution Simulation and Validation of Soil Moisture in the Arid Region of Northwest China. *Sci. Rep.* **2019**, *9*, 17227. [CrossRef] [PubMed]
22. Swenson, S.C.; Lawrence, D.M.; Lee, H. Improved Simulation of the Terrestrial Hydrological Cycle in Permafrost Regions by the Community Land Model. *J. Adv. Model. Earth Syst.* **2012**, *4*, M08002. [CrossRef]
23. Rasheed, M.W.; Tang, J.; Sarwar, A.; Shah, S.; Saddique, N.; Khan, M.U.; Imran Khan, M.; Nawaz, S.; Shamshiri, R.R.; Aziz, M.; et al. Soil Moisture Measuring Techniques and Factors Affecting the Moisture Dynamics: A Comprehensive Review. *Sustainability* **2022**, *14*, 11538. [CrossRef]
24. Zhao, T.; Shi, J.; Lv, L.; Xu, H.; Chen, D.; Cui, Q.; Jackson, T.J.; Yan, G.; Jia, L.; Chen, L.; et al. Soil Moisture Experiment in the Luan River Supporting New Satellite Mission Opportunities. *Remote Sens. Environ.* **2020**, *240*, 111680. [CrossRef]
25. Vather, T.; Everson, C.S.; Franz, T.E. The Applicability of the Cosmic Ray Neutron Sensor to Simultaneously Monitor Soil Water Content and Biomass in an *Acacia mearnsii* Forest. *Hydrology* **2020**, *7*, 48. [CrossRef]
26. Pauwels, V.R.N.; Hoeben, R.; Verhoest, N.E.C.; De Troch, F.P.; Troch, P.A. Improvement of TOPLATS-Based Discharge Predictions through Assimilation of ERS-Based Remotely Sensed Soil Moisture Values. *Hydrol. Process.* **2002**, *16*, 995–1013. [CrossRef]
27. Brocca, L.; Moramarco, T.; Melone, F.; Wagner, W.; Hasenauer, S.; Hahn, S. Assimilation of Surface- and Root-Zone ASCAT Soil Moisture Products into Rainfall–Runoff Modeling. *IEEE Trans. Geosci. Remote Sens.* **2012**, *50*, 2542–2555. [CrossRef]

28. Fairbairn, D.; Barbu, A.L.; Napoly, A.; Albergel, C.; Mahfouf, J.-F.; Calvet, J.-C. The Effect of Satellite-Derived Surface Soil Moisture and Leaf Area Index Land Data Assimilation on Streamflow Simulations over France. *Hydrol. Earth Syst. Sci.* **2017**, *21*, 2015–2033. [CrossRef]

29. Reichle, R.H.; Walker, J.P.; Koster, R.D.; Houser, P.R. Extended versus Ensemble Kalman Filtering for Land Data Assimilation. *J. Hydrometeorol.* **2002**, *3*, 728–740. [CrossRef]

30. Draper, C.; Mahfouf, J.-F.; Calvet, J.-C.; Martin, E.; Wagner, W. Assimilation of ASCAT Near-Surface Soil Moisture into the SIM Hydrological Model over France. *Hydrol. Earth Syst. Sci.* **2011**, *15*, 3829–3841. [CrossRef]

31. de Rosnay, P.; Drusch, M.; Vasiljevic, D.; Balsamo, G.; Albergel, C.; Isaksen, L. A simplified extended Kalman filter for the global operational soil moisture analysis at ECMWF. *Q. J. R. Meteorol. Soc.* **2013**, *139*, 1199–1213. [CrossRef]

32. Barbu, A.L.; Calvet, J.-C.; Mahfouf, J.-F.; Albergel, C.; Lafont, S. Assimilation of Soil Wetness Index and Leaf Area Index into the ISBA-A-gs Land Surface Model: Grassland Case Study. *Biogeosciences* **2011**, *8*, 1971–1986. [CrossRef]

33. Masson, V.; Le Moigne, P.; Martin, E.; Faroux, S.; Alias, A.; Alkama, R.; Belamari, S.; Barbu, A.; Boone, A.; Bouyssel, F.; et al. The SURFEXv7.2 Land and Ocean Surface Platform for Coupled or Offline Simulation of Earth Surface Variables and Fluxes. *Geosci. Model Dev.* **2013**, *6*, 929–960. [CrossRef]

34. Albergel, C.; Munier, S.; Leroux, D.J.; Dewaele, H.; Fairbairn, D.; Barbu, A.L.; Gelati, E.; Dorigo, W.; Faroux, S.; Meurey, C.; et al. Sequential Assimilation of Satellite-Derived Vegetation and Soil Moisture Products Using SURFEX_v8.0: LDAS-Monde Assessment over the Euro-Mediterranean Area. *Geosci. Model Dev.* **2017**, *10*, 3889–3912. [CrossRef]

35. Seity, Y.; Brousseau, P.; Malardel, S.; Hello, G.; Bénard, P.; Bouttier, F.; Lac, C.; Masson, V. The AROME-France Convective-Scale Operational Model. *Mon. Weather Rev.* **2011**, *139*, 976–991. [CrossRef]

36. Brousseau, P.; Seity, Y.; Ricard, D.; Léger, J. Improvement of the forecast of convective activity from the AROME-France system. *Q. J. R. Meteor. Soc.* **2016**, *142*, 2231–2243. [CrossRef]

37. Calvet, J.-C.; Gibelin, A.-L.; Roujean, J.-L.; Martin, E.; Le Moigne, P.; Douville, H.; Noilhan, J. Past and Future Scenarios of the Effect of Carbon Dioxide on Plant Growth and Transpiration for Three Vegetation Types of Southwestern France. *Atmos. Chem. Phys.* **2008**, *8*, 397–406. [CrossRef]

38. Decharme, B.; Boone, A.; Delire, C.; Noilhan, J. Local Evaluation of the Interaction between Soil Biosphere Atmosphere Soil Multilayer Diffusion Scheme Using Four Pedotransfer Functions. *J. Geophys. Res. D Atmos.* **2011**, *116*, D20126. [CrossRef]

39. Boone, A.; Masson, V.; Meyers, T.; Noilhan, J. The Influence of the Inclusion of Soil Freezing on Simulations by a Soil–Vegetation–Atmosphere Transfer Scheme. *J. Appl. Meteorol.* **2000**, *39*, 1544–1569. [CrossRef]

40. Faroux, S.; Kaptué Tchuenté, A.T.; Roujean, J.-L.; Masson, V.; Martin, E.; Le Moigne, P. ECOCLIMAP-II/Europe: A Twofold Database of Ecosystems and Surface Parameters at 1 Km Resolution Based on Satellite Information for Use in Land Surface, Meteorological and Climate Models. *Geosci. Model Dev.* **2013**, *6*, 563–582. [CrossRef]

41. Mucia, A.; Bonan, B.; Albergel, C.; Zheng, Y.; Calvet, J.-C. Assimilation of Passive Microwave Vegetation Optical Depth in LDAS-Monde: A Case Study over the Continental USA. *Biogeosciences* **2022**, *19*, 2557–2581. [CrossRef]

42. Mucia, A.; Bonan, B.; Zheng, Y.; Albergel, C.; Calvet, J.-C. From Monitoring to Forecasting Land Surface Conditions Using a Land Data Assimilation System: Application over the Contiguous United States. *Remote Sens.* **2020**, *12*, 2020. [CrossRef]

43. Leroux, D.J.; Calvet, J.-C.; Munier, S.; Albergel, C. Using Satellite-Derived Vegetation Products to Evaluate LDAS-Monde over the Euro-Mediterranean Area. *Remote Sens.* **2018**, *10*, 1199. [CrossRef]

44. Albergel, C.; Munier, S.; Bocher, A.; Bonan, B.; Zheng, Y.; Draper, C.; Leroux, D.J.; Calvet, J.-C. LDAS-Monde Sequential Assimilation of Satellite Derived Observations Applied to the Contiguous US: An ERA-5 Driven Reanalysis of the Land Surface Variables. *Remote Sens.* **2018**, *10*, 1627. [CrossRef]

45. Reichle, R.H.; Koster, R.D. Bias Reduction in Short Records of Satellite Soil Moisture. *Geophys. Res. Lett.* **2004**, *31*, L19501. [CrossRef]

46. Drusch, M.; Wood, E.F.; Gao, H. Observation Operators for the Direct Assimilation of TRMM Microwave Imager Retrieved Soil Moisture. *Geophys. Res. Lett.* **2005**, *32*, L15403. [CrossRef]

47. Scipal, K.; Holmes, T.; de Jeu, R.; Naeimi, V.; Wagner, W. A Possible Solution for the Problem of Estimating the Error Structure of Global Soil Moisture Data Sets. *Geophys. Res. Lett.* **2008**, *35*, L24403. [CrossRef]

48. Barbu, A.L.; Calvet, J.-C.; Mahfouf, J.-F.; Lafont, S. Integrating ASCAT Surface Soil Moisture and GEOV1 Leaf Area Index into the SURFEX Modelling Platform: A Land Data Assimilation Application over France. *Hydrol. Earth Syst. Sci.* **2014**, *18*, 173–192. [CrossRef]

49. Massari, C.; Brocca, L.; Tarpanelli, A.; Moramarco, T. Data Assimilation of Satellite Soil Moisture into Rainfall-Runoff Modelling: A Complex Recipe? *Remote Sens.* **2015**, *7*, 11403–11433. [CrossRef]

50. Baret, F.; Weiss, M.; Lacaze, R.; Camacho, F.; Makhmara, H.; Pacholcyzk, P.; Smets, B. GEOV1: LAI and FAPAR Essential Climate Variables and FCOVER Global Time Series Capitalizing over Existing Products. Part1: Principles of Development and Production. *Remote Sens. Environ.* **2013**, *137*, 299–309. [CrossRef]

51. Meier, J.; Zabel, F.; Mauser, W. A Global Approach to Estimate Irrigated Areas—A Comparison between Different Data and Statistics. *Hydrol. Earth Syst. Sci.* **2018**, *22*, 1119–1133. [CrossRef]

52. Calvet, J.-C.; Fritz, N.; Berne, C.; Piguet, B.; Maurel, W.; Meurey, C. Deriving pedotransfer functions for soil quartz fraction in southern France from reverse modelling. *Soil* **2016**, *2*, 615–629. [CrossRef]

53. Zhang, S.; Calvet, J.-C.; Darrozes, J.; Roussel, N.; Frappart, F.; Bouhours, G. Deriving surface soil moisture from reflected GNSS signal observations over a grassland site in southwestern France. *Hydrol. Earth Syst. Sci.* **2018**, *22*, 1931–1946. [CrossRef]
54. Ceballos, A.; Scipal, K.; Wagner, W.; Martínez-Fernández, J. Validation of ERS Scatterometer-Derived Soil Moisture Data in the Central Part of the Duero Basin, Spain. *Hydrol. Process.* **2005**, *19*, 1549–1566. [CrossRef]
55. Sanchez, N.; Martinez-Fernandez, J.; Scaini, A.; Perez-Gutierrez, C. Validation of the SMOS L2 Soil Moisture Data in the REMEDHUS Network (Spain). *IEEE Trans. Geosci. Remote Sens.* **2012**, *50*, 1602–1611. [CrossRef]
56. Wagner, W.; Pathe, C.; Doubkova, M.; Sabel, D.; Bartsch, A.; Hasenauer, S.; Blöschl, G.; Scipal, K.; Martínez-Fernández, J.; Löw, A. Temporal Stability of Soil Moisture and Radar Backscatter Observed by the Advanced Synthetic Aperture Radar (ASAR). *Sensors* **2008**, *8*, 1174–1197. [CrossRef] [PubMed]
57. Gonzalez-Zamora, A.; Sanchez, N.; Pablos, M.; Martinez-Fernandez, J. CCI soil moisture assessment with SMOS soil moisture and in situ data under different environmental conditions and spatial scales in Spain. *Remote Sens. Environ.* **2018**, *225*, 469–482. [CrossRef]
58. Dorigo, W.; Himmelbauer, I.; Aberer, D.; Schremmer, L.; Petrakovic, I.; Zappa, L.; Preimesberger, W.; Xaver, A.; Annor, F.; Ardö, J.; et al. The International Soil Moisture Network: Serving Earth system science for over a decade. *Hydrol. Earth Syst. Sci.* **2021**, *25*, 5749–5804. [CrossRef]
59. Owe, M.; Van de Griend, A.A. Comparison of soil moisture penetration depths for several bare soils at two microwave frequencies and implications for remote sensing. *Water Resour. Res.* **1998**, *34*, 2319–2327. [CrossRef]
60. Albergel, C.; Zheng, Y.; Bonan, B.; Dutra, E.; Rodríguez-Fernández, N.; Munier, S.; Draper, C.; de Rosnay, P.; Muñoz-Sabater, J.; Balsamo, G.; et al. Data assimilation for continuous global assessment of severe conditions over terrestrial surfaces. *Hydrol. Earth Syst. Sci.* **2020**, *24*, 4291–4316. [CrossRef]
61. Blauhut, V.; Stoelzle, M.; Ahopelto, L.; Brunner, M.I.; Teutschbein, C.; Wendt, D.E.; Akstinas, V.; Bakke, S.J.; Barker, L.J.; Bartošová, L.; et al. Lessons from the 2018–2019 European Droughts: A Collective Need for Unifying Drought Risk Management. *Nat. Hazards Earth Syst. Sci.* **2022**, *22*, 2201–2217. [CrossRef]
62. EEA. Soil Moisture Dash Board, European Environment Agency. 2019. Available online: https://www.eea.europa.eu/data-and-maps/data/data-viewers/soil-moisture (accessed on 30 August 2023).
63. Liu, Y.; Yang, Y.; Yue, X. Evaluation of satellite-based soil moisture products over four different continental in-situ measurements. *Remote Sens.* **2018**, *10*, 1161. [CrossRef]
64. Feng, S.; Huang, X.; Zhao, S.; Qin, Z.; Fan, J.; Zhao, S. Evaluation of Several Satellite-Based Soil Moisture Products in the Continental US. *Sensors* **2022**, *22*, 9977. [CrossRef] [PubMed]
65. Sishah, S.; Abraham, T.; Azene, G.; Dessalew, A.; Hundera, H. Downscaling and Validating SMAP Soil Moisture Using a Machine Learning Algorithm over the Awash River Basin, Ethiopia. *PLoS ONE* **2023**, *18*, e0279895. [CrossRef] [PubMed]
66. El Hajj, M.; Baghdadi, N.; Zribi, M.; Rodríguez-Fernández, N.; Wigneron, J.P.; Al-Yaari, A.; Al Bitar, A.; Albergel, C.; Calvet, J.-C. Evaluation of SMOS, SMAP, ASCAT and Sentinel-1 soil moisture products at sites in southwestern France. *Remote Sens.* **2018**, *10*, 569. [CrossRef]
67. Portal, G.; Jagdhuber, T.; Vall-llossera, M.; Camps, A.; Pablos, M.; Entekhabi, D.; Piles, M. Assessment of multi-scale SMOS and SMAP soil moisture products across the Iberian peninsula. *Remote Sens.* **2020**, *12*, 570. [CrossRef]
68. Tall, M.; Albergel, C.; Bonan, B.; Zheng, Y.; Guichard, F.; Dramé, M.S.; Gaye, A.T.; Sitondji, L.O.; Hountondji, F.C.C.; Nikiema, P.M.; et al. Towards a long-term reanalysis of land surface variables over western Africa: LDAS-Monde applied over Burkina Faso from 2001 to 2018. *Remote Sens.* **2019**, *11*, 735. [CrossRef]
69. Capehart, W.; Carlson, T. Decoupling of surface and near-surface soil water content: A remote sensing perspective. *Water Resour. Res.* **1997**, *33*, 1383–1395. [CrossRef]
70. Bonan, B.; Albergel, C.; Zheng, Y.; Barbu, A.L.; Fairbairn, D.; Munier, S.; Calvet, J.-C. An Ensemble Square Root Filter for the Joint Assimilation of Surface Soil Moisture and Leaf Area Index within the Land Data Assimilation System LDAS-Monde: Application over the Euro-Mediterranean Region. *Hydrol. Earth Syst. Sci.* **2020**, *24*, 325–347. [CrossRef]
71. Bazzi, H.; Baghdadi, N.; El Hajj, M.; Zribi, M.; Belhouchette, H. A Comparison of Two Soil Moisture Products S2MP and Copernicus-SSM over Southern France. *IEEE J. Sel. Top. Appl. Earth Obs. Remote Sens.* **2019**, *12*, 3366–3375. [CrossRef]
72. Modanesi, S.; Massari, C.; Bechtold, M.; Lievens, H.; Tarpanelli, A.; Brocca, L.; Zappa, L.; De Lannoy, G.J.M. Challenges and benefits of quantifying irrigation through the assimilation of Sentinel-1 backscatter observations into Noah-MP. *Hydrol. Earth Syst. Sci.* **2022**, *26*, 4685–4706. [CrossRef]
73. Draper, C.S.; Reichle, R.H.; De Lannoy, G.J.M.; Liu, Q. Assimilation of Passive and Active Microwave Soil Moisture Retrievals. *Geophys. Res. Lett.* **2012**, *39*, L04401. [CrossRef]
74. Wagner, W.; Lindorfer, R.; Melzer, T.; Hahn, S.; Bauer-Marschallinger, B.; Morrison, K.; Calvet, J.C.; Hobbs, S.; Quast, R.; Greimeister-Pfeil, I.; et al. Widespread occurrence of anomalous C-band backscatter signals in arid environments caused by subsurface scattering. *Remote Sens. Environ.* **2022**, *276*, 113025. [CrossRef]
75. Shamambo, D.; Bonan, B.; Calvet, J.-C.; Albergel, C.; Hahn, S. Interpretation of ASCAT radar scatterometer observations over land: A case study over southwestern France. *Remote Sens.* **2019**, *11*, 2842. [CrossRef]